**THE EUROPEAN
PHYSICAL JOURNAL D**

Regular Article

Accurate treatment of total photoabsorption cross sections by an ab initio time-dependent method

Mohammad Noh Daud[a]

Department of Chemistry, University of Malaya, 50603 Kuala Lumpur, Malaysia

Abstract. A detailed discussion of parallel and perpendicular transitions required for the photoabsorption of a molecule is presented within a time-dependent view. Total photoabsorption cross sections for the first two ultraviolet absorption bands of the N_2O molecule corresponding to transitions from the X^1A' state to the $2^1A'$ and $1^1A''$ states are calculated to test the reliability of the method. By fully considering the property of the electric field polarization vector of the incident light, the method treats the coupling of angular momentum and the parity differently for two kinds of transitions depending on the direction of the vector whether it is: (a) situated parallel in a molecular plane for an electronic transition between states with the same symmetry; (b) situated perpendicular to a molecular plane for an electronic transition between states with different symmetry. Through this, for those transitions, we are able to offer an insightful picture of the dynamics involved and to characterize some new aspects in the photoabsorption process of N_2O. Our calculations predicted that the parallel transition to the $2^1A'$ state is the major dissociation pathway which is in qualitative agreement with the experimental observations. Most importantly, a significant improvement in the absolute value of the total cross section over previous theoretical results [R. Schinke, J. Chem. Phys. **134**, 064313 (2011), M.N. Daud, G.G. Balint-Kurti, A. Brown, J. Chem. Phys. **122**, 054305 (2005), S. Nanbu, M.S. Johnson, J. Phys. Chem. A **108**, 8905 (2004)] was obtained.

1 Introduction

An exact time-dependent quantum wave packet approach has been used to study the dynamics of a molecule by solving numerically the time-dependent Schrödinger equation. A nuclear ground state wave function is initially projected onto an upper electronic excited state potential and the resulting wave packet is propagated towards the exit channel. The approach has been developed in several ways in the past 30 years in studying some of the important molecular gases from the simplest diatomic up to tetratomic molecules [1–8]. Although the exact solution of the time-dependent approach for large molecules requires multiple extra dimensions of matrix multiplications, it has a great compensating advantage of immediately yielding the energy dependence of cross sections and other physical observables. A well-known formula of total photoabsorption cross section [1] is given by:

$$\sigma(E) = N(\nu) \int_0^\infty \exp\left(\frac{iE_f t}{\hbar}\right) \langle \Phi(t_i) | \Phi(t) \rangle \, dt \quad (1)$$

where $N(\nu) = 2\pi^2 \nu / \hbar c \epsilon_0$, ν is the frequency of incident light, E_f is the final energy, $\Phi(t_i)$ is the initial wave packet

at $t = 0$ and $\Phi(t)$ is the wave packet at $t > 0$. Thus, once $\langle \Phi(t_i) | \Phi(t) \rangle$ is known and Fourier transformed, the cross section at all frequencies can be obtained.

A correct treatment of angular momentum in preparing the initial wave packet $\Phi(t_i)$ is introduced which relies on the properties of the vector components of the transition dipole moment. The method is based on our previous paper [9] but has been carefully revised in many ways in order to ensure the final form of $\Phi(t_i)$ is correct. The method has been applied to calculate the cross section of two absorption bands of nitrous oxide (N_2O), involving transitions to two lowest excited state potentials. The transitions are only allowed when N_2O is bent where the electronic states are assigned in this geometry as X^1A' for the ground state and as $1^1A''$ and $2^1A'$ for the first and second excited states. The symmetry of the states can be described in terms of C_s, an irreducible representation and its most stable electronic configuration has orbital occupancies of $(1a')^2(2a')^2(3a')^2(4a')^2(5a')^2(6a')^2(1a'')^2(7a')^2(8a')^2 (2a'')^2(9a')^2$. The singlet channel is the main dissociation pathway that produces rotationally hot but vibrationally cold N_2 [10–12]. In addition to these, the fact that the measured anisotropy parameter (β) values did not correspond to either of the limiting values ($\beta = -1$ or 2) was taken to indicate that the parallel transition is not
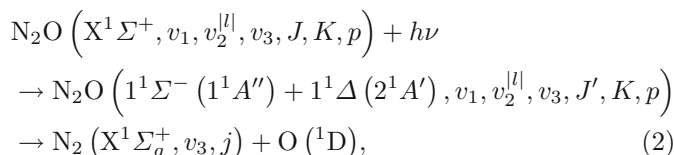
ᵃ e-mail: mnoh@um.edu.my
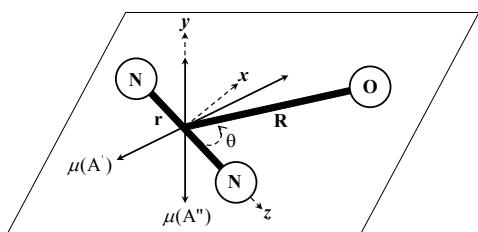
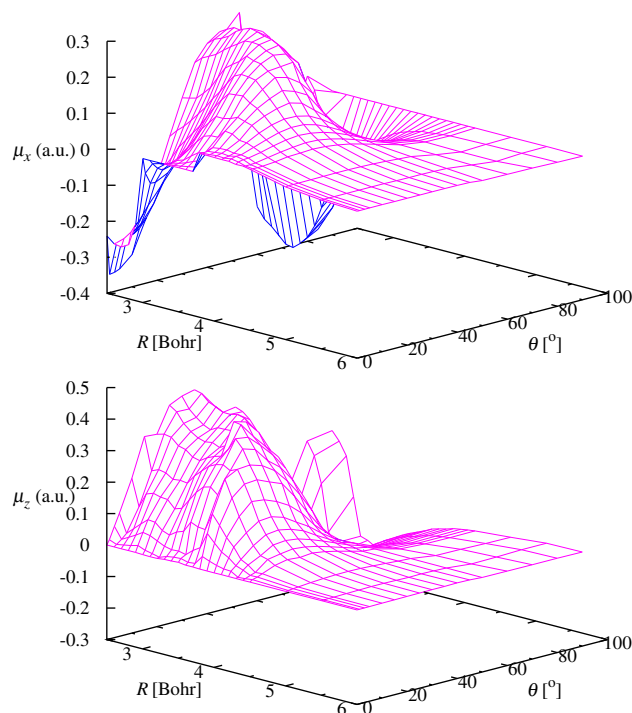**Fig. 1.** Jacobi and Cartesian coordinates used in the electronic structure and dynamics calculations.
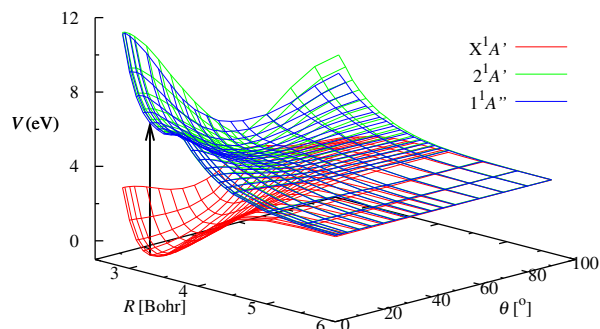
Fig. 2. Three dimensional plot of the three lowest singlet electronic potential energy surfaces of N_2O at a fixed ground state equilibrium geometry of $r = 2.13199$ Bohr. The energies are plotted relative to the minimum of the ground electronic state, X^1A'.

Fig. 3. Three dimensional plot of the two components of transition dipole moment surfaces for the $X^1A' \rightarrow 2^1A'$ transition at a fixed ground state equilibrium geometry of $r = 2.13199$ Bohr.

Fig. 4. Three dimensional plot of the component of transition dipole moment surface for the $X^1A' \rightarrow 1^1A''$ transition at a fixed ground state equilibrium geometry of $r = 2.13199$ Bohr.

the only excitation pathway, and that the perpendicular transition was also involved [10–18]. The overall photoabsorption processes can be described by:
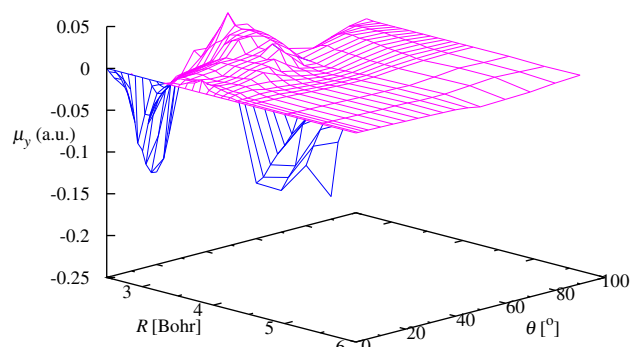
$$N_2O \left(X^1\Sigma^+, v_1, v_2^{|l|}, v_3, J, K, p\right) + h\nu$$

$$\rightarrow N_2O \left(1^1\Sigma^- \left(1^1A''\right) + 1^1\Delta \left(2^1A'\right), v_1, v_2^{|l|}, v_3, J', K, p\right)$$

$$\rightarrow N_2 \left(X^1\Sigma_g^+, v_3, j\right) + O \left(^1D\right), \qquad (2)$$

where J is the total angular momentum quantum number, K is the quantum number for the projection of **J** on the body-fixed z axis, p is the parity which describes the property of the system under inversion of all the space-fixed coordinates, j is the rotational quantum number of the diatomic photofragment product and v_1, v_2, v_3 are vibrational quanta for the N_2-O stretching and bending, and N-NO stretching, respectively. Furthermore, the notation of $(v_1, v_2^{|l|}, v_3)$ has been thoroughly used to denote the degenerate states of (v_1, v_2, v_3) where the allowed values of vibrational angular momentum l are related with v_2 by $l = -v_2, -v_2+2, \ldots, +v_2$. Whereas the allowed values of J are related with l by $J = |l|, |l|+1, \ldots$.

Using the AVQZ basis set [19], the state-averaged complete active space self-consistent field (CASSCF) method followed by the internally contracted multireference configuration interaction (MRCI) method [20] has been performed to compute the potential energies of the X^1A', $2^1A'$ and $1^1A''$ states. Figure 1 displays the N_2O molecule defined in the Jacobi coordinates system (R, r, θ) and its relation with the transition dipole moment vector in body-fixed Cartesian coordinates (x, y, z). Figure 2 shows the

potential energy surfaces of X^1A', $2^1A'$ and $1^1A''$ states. It is clear that the $2^1A'(^1\Delta)$ and $1^1A''(^1\Sigma^-)$ states represent the first and second absorption bands of N_2O. Dipole transitions from the ground $^1\Sigma^+$ state to the excited $^1\Sigma^-$ and $^1\Delta$ states are forbidden in linear geometry, but weakly allowed for bent geometries. Figure 3 shows the μ_x and μ_z components of the transition dipole moment connecting between the ground X^1A' and excited $2^1A'$ state potentials. While, Figure 4 shows the μ_y component of the transition dipole moment connecting between the ground X^1A' and excited $1^1A''$ state potentials.

This paper outlines the theoretical and numerical frameworks in great detail in the first section by taking into account the coupling of angular momentum and

the parity of the molecule. The theoretical results are discussed in the second section and comparisons are made with experimental findings whenever available. The final section concludes this work briefly.

2 Theoretical and numerical aspects

2.1 Basis expansion and Hamiltonian operator

Before we begin formulating the initial wave packet, a nuclear wave function has to be constructed within the Born-Oppenheimer approximation in the following form [21,22]

$$\Psi_M^J (R, r, \theta, \omega) = \sqrt{\frac{2J+1}{8\pi^2}} \sum_{K=-J}^{J} \psi_K^J (R, r, \theta)$$
$$\times D_{K,M}^J (\omega) \qquad (3)$$

where M is the quantum number for the projection of $\mathbf{J}$ on the space-fixed Z axis, $D_{K,M}^J$ is the Wigner D-function [21,22] and $\omega \equiv \alpha, \beta, \gamma$ are the Euler angles. Thus, the $D_{K,M}^J$ and $D_{-K,M}^J$ terms in equation (3) can be grouped together to define a parity-adapted angular momentum basis function,

$$\Lambda_{K,M}^{J,p}(\omega) = \frac{1}{4\pi} \sqrt{\frac{2J+1}{(1+\delta_{0,K})}}$$
$$\times \left[D_{K,M}^J (\omega) + (-1)^{J+K+p} D_{-K,M}^J (\omega) \right] \quad (4)$$

where $p = 1$ represents a state of odd parity and $p = 2$ represents a state of even parity. For a given J, there exist $2J + 1$ wave functions which correspond to different K. The K and $-K$ terms have been grouped together in one parity-adapted basis function. Accordingly, the $2J + 1$ fold degenerate of K states can now be divided into a set of $J + 1$ fold degenerates with $K = 0, 1, 2, 3, \ldots, J$ for $p = 2$ and a set of J fold degenerate states with $K = 1, 2, 3, \ldots, J$ for $p = 1$.

In order to solve the eigen equation of the triatomic molecule using basis function (3), the following nuclear non-adiabatic Hamiltonian operator was used [23,24]

$$\hat{H} = -\hbar^2/2 \Bigg\{ \left(m^{-1} D_R^2 + m_r^{-1} D_r^2 \right)$$
$$+ \left(m^{-1} R^{-2} + m_r^{-1} r^{-2} \right) \left(D_\theta^2 - K^2 \sin^{-2}\theta \right)$$
$$+ m^{-1} R^{-2} \Big[[J(J+1) - K(K+1)]^{1/2} (D_\theta - K \cot\theta)$$
$$+ [J(J+1) - K(K-1)]^{1/2} (-D_\theta - K \cot\theta)$$
$$+ \left(J(J+1) - 2K^2 \right) \Big] \Bigg\} + V(R, r, \theta) \quad (5)$$

where $D_i = \partial/\partial i$, $m = m_{N_2} m_O / m_{N_2O}$, $m_r = m_N^2 / m_{N_2}$ and V is the potential energy of inter-electronic repulsion and electron-nucleus attraction. For simplification, the N-N internuclear distance r was fixed at its equilibrium geometry, 2.13199 Bohr. The justification of using

the two-dimensional model is based on the fact that the N-N bond distance contracts less than 3% from 2.13199 Bohr in N_2O to 2.07416 Bohr in N_2 following dissociation.

The action of the radial kinetic energy operator on the nuclear wave function is evaluated using fast Fourier transforms where the operator is diagonal in momentum space [3,4]. The action of the angular kinetic energy operator on the wave function is performed by expanding the wave function in (3) in terms of normalised associated Legendre polynomials $\Theta_{j,K}(\theta)$. Consequently, the grid representation of the angular variable can be described by a N_α Gauss-Legendre quadrature scheme [3,4] where the maximum value of j in the associated basis representation is $j_{\max} = (N_\alpha - 1)$. Using all the facts and the parity-adapted basis functions $\Lambda_{K,M}^{J,p}$, the wave function in equation (3) is rewritten to be:

$$\Psi_M^{J,p} (R, r, \theta, \omega) = \sum_{K=\lambda}^{J} \sum_{j=K}^{j_{\max}} \psi_K^{J,p} (R, r) \Theta_{j,K}(\theta)$$
$$\times \Lambda_{K,M}^{J,p}(\omega) \quad (6)$$

where λ is defined as:

$$\lambda = \frac{1 - (-1)^{J+p}}{2}, \quad (7)$$

and $\lambda = K_{\min}$ can take a value of 0 or 1, depending on the value of $(-1)^{J+p}$. For $K \neq 0$, p can take a value of 1 or 2. For $K = 0$, p can take only a value of 2 because if $J = 0$, the only possible value of λ is 0. A uniform grid was used for the coordinates R and θ in evaluating $\psi_K^{J,p}$ on the grid points based upon the ground state potential energy surface, X^1A'.

To compute the rotational-vibrational energy and wave function for the state with odd bending quantum number, we considered $J = 1$ with parity state either odd ($p = 1$) or even ($p = 2$). For an odd parity state, the allowed K values are 0 and 1, while for an even parity state the allowed K value is 0. For even bending quantum number, we considered $J = 0$ with even parity in the calculations. $J = 0$ with odd parity is forbidden by symmetry and in this case, the allowed K value is 0. Since J and parity are good quantum numbers, the calculations were performed separately for different values of J and parity. On the other hand, K is not a good quantum number and different values of K are coupled.

The computed and experimentally observed vibrational energies for the lowest six states of N_2O are tabulated in Table 1. The assignments of the states were made by visual inspection of the vibrational wave functions. As an example, we display in Figure 5, the wave function contour plots corresponding to the ground, pure bending, pure stretching and coupled bending-stretching vibrations, with one of the internal coordinates kept fixed at its equilibrium value. In general, the agreement between the computed and the experimental values is quite good, with maximum discrepancy of 20.97 cm^{-1} arising from the $(0,3^1,0)$ vibrational state. Therefore, the ground state wave functions should be of sufficient quality to proceed to study the photoabsorption process of N_2O.

Table 1. Comparison between computed and experimental rotational-vibrational energies (cm^{-1}) for the X$^1A'$ ground electronic state of N$_2$O molecule.

$v_1, v_2^{|l|}, v_3$	ΔE_i(Theory)^a	ΔE(Experimental)^b
$0,0^0,0$	0.00	0.00
$0,1^1,0$	583.67	588.77
$0,2^0,0$	1160.23	1168.13
$1,0^0,0$	1269.77	1284.90
$0,3^1,0$	1728.10	1749.07
$1,1^1,0$	1894.98	1880.27

^{a} ΔE_i(Theory) $= E_i(v_1, v_2^{|l|}, v_3) - E_i(0, 0^0, 0)$.
^{b} The experimental values were taken from references [25–27].
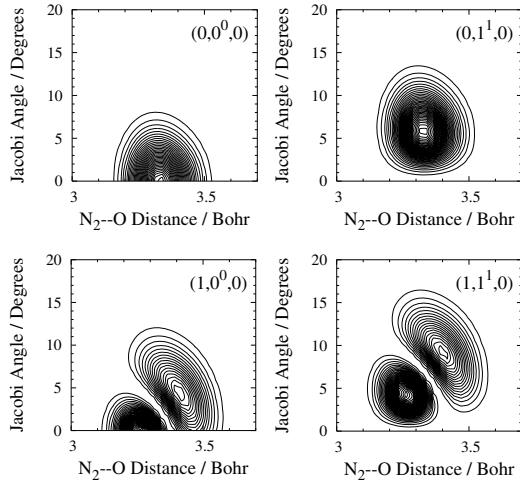
Fig. 5. Contour plots of the rotational-vibrational wave functions for the X$^1A'$ ground electronic state of the N$_2$O molecule.

2.2 Initial wave packet

The initial wave packet in equation (1) in the space-fixed frame can be written explicitly in the form of

$$|\Phi(R,r,\theta,\omega,t_i)\rangle = \boldsymbol{\mu} \cdot \boldsymbol{\epsilon}_m \ |\Psi_M^{J,p}(R,r,\theta,\omega)\rangle \qquad (8)$$

where $\boldsymbol{\mu}$ is the transition dipole moment vector, connecting different electronic states and $\boldsymbol{\epsilon}_m$ is the electric field polarization vector of the polarized light. Thus, $\boldsymbol{\epsilon}_m$ can been defined in terms of complex unit vectors [21,22]

$$\boldsymbol{\epsilon}_{-1} = \frac{1}{\sqrt{2}}(\boldsymbol{\epsilon}_x - i\boldsymbol{\epsilon}_y), \qquad \boldsymbol{\epsilon}_{+1} = -\frac{1}{\sqrt{2}}(\boldsymbol{\epsilon}_x + i\boldsymbol{\epsilon}_y),$$
$$\boldsymbol{\epsilon}_0 = \boldsymbol{\epsilon}_z , \qquad (9)$$

where $m = \pm 1$ corresponds to circularly and $m = 0$ corresponds to linearly polarized light, respectively. $\boldsymbol{\mu}$ is related to the Cartesian components of $\boldsymbol{\epsilon}_m$ by equation

$$\boldsymbol{\mu} = \mu_x \boldsymbol{\epsilon}_x + \mu_y \boldsymbol{\epsilon}_y + \mu_z \boldsymbol{\epsilon}_z. \qquad (10)$$

The property of the initial wave packet rely on the projection of the polarization vector of the light onto the plane of the molecule. If the vector lies in the xz plane, the so-called parallel transition, equation (9) becomes

$$\boldsymbol{\epsilon}_{-1} = \frac{1}{\sqrt{2}}\boldsymbol{\epsilon}_x, \qquad \boldsymbol{\epsilon}_0 = \boldsymbol{\epsilon}_z, \qquad \boldsymbol{\epsilon}_{+1} = -\frac{1}{\sqrt{2}}\boldsymbol{\epsilon}_x, \quad (11)$$

where $\boldsymbol{\epsilon}_y = 0$. Meanwhile, if the vector lies along the y-axis, the so-called perpendicular transition, equation (9) becomes

$$\boldsymbol{\epsilon}_{-1} = \frac{1}{\sqrt{2}} - i\boldsymbol{\epsilon}_y, \qquad \boldsymbol{\epsilon}_0 = 0, \qquad \boldsymbol{\epsilon}_{+1} = -\frac{1}{\sqrt{2}}i\boldsymbol{\epsilon}_y, \quad (12)$$

where $\boldsymbol{\epsilon}_x = \boldsymbol{\epsilon}_z = 0$.

Defining $\boldsymbol{\epsilon}_m$ to be parallel to $\boldsymbol{\mu}$, equation (8) can be written in terms of its components in the space-fixed frame,

$$|\Phi(R,r,\theta,\omega,t_i)\rangle = \mu_m \ |\Psi_M^{J,p}(R,r,\theta,\omega)\rangle . \qquad (13)$$

Equation (13) can be transformed into its body-fixed frame,

$$|\Phi(R,r,\theta,\omega,t_i)\rangle = \sum_{n=-1}^{1} \mu_n D_{n,m}^1(\omega)$$
$$\times |\Psi_M^{J,p}(R,r,\theta,\omega)\rangle \qquad (14)$$

by using the Wigner D-function $D_{n,m}^1(\omega)$ as a rotation matrix for transformation between the two frames where μ_n are the components of $\boldsymbol{\mu}$ in the body-fixed frame. Making use of equation (6) and the following Clebsch-Gordan series [21,22]

$$D_{n,m}^1(\omega)D_{\pm K,M}^J(\omega) = \sum_{J'=J-1}^{J+1} \langle 1, m : J, M | J', m+M \rangle$$
$$\times \langle 1, n : J, \pm K | J', n \pm K \rangle$$
$$\times D_{n\pm K, m+M}^{J'}(\omega) \qquad (15)$$

where

$$\langle 1, m : J, M | J', m+M \rangle$$

and

$$\langle 1, n : J, \pm K | J', n \pm K \rangle$$

are Clebsch-Gordan coefficients [21,22], the initial wave packet in equation (14) can be written in the form of:

$$|\Phi^{J,p}(R,r,\theta,\omega,t_i)\rangle = \sum_{J'=J-1}^{J+1} \langle 1, m : J, M | J', m+M \rangle$$
$$\times \sum_{K=\lambda}^{J} \sum_{j=K}^{j_{max}} |\psi_K^{J,p}(R,r)\rangle \ |\varphi_{K,M}^{J',J,p}(\theta,\omega)\rangle$$
$$(16)$$

where

$$|\varphi_{K,M}^{J',J,p}(\theta,\omega)\rangle = \frac{1}{4\pi}\sqrt{\frac{2J+1}{(1+\delta_{0,K})}}|\Theta_{j,K}(\theta)\rangle$$

$$\times \Big\{ \mu_{-1}\Big[D_{-1+K,m+M}^{J'}(\omega)$$

$$\times \langle 1,-1:J,K|J',-1+K\rangle$$

$$+ (-1)^{J+K+p} D_{-1-K,m+M}^{J'}(\omega)$$

$$\times \langle 1,-1:J,-K|J',-1-K\rangle \Big]$$

$$+ \mu_0\Big[D_{K,m+M}^{J'}(\omega)\langle 1,0:J,K|J',K\rangle$$

$$+ (-1)^{J+K+p} D_{-K,m+M}^{J'}(\omega)$$

$$\times \langle 1,0:J,-K|J',-K\rangle]$$

$$+ \mu_1\Big[D_{1+K,m+M}^{J'}(\omega)\langle 1,1:J,K|J',1+K\rangle$$

$$+ (-1)^{J+K+p} D_{1-K,m+M}^{J'}(\omega)$$

$$\times \langle 1,1:J,-K|J',1-K\rangle \Big]\Big\}. \quad (17)$$

Summation $\sum_{J'=J-1}^{J+1}$ in equation (16) indicates that the transition obeys the general rotational selection rule for an electric dipole transition $\Delta J = 0, \pm 1$ where the transition from $J = 0$ to $J' = 0$ is forbidden by symmetry. Accordingly, the initial wave packet $|\Phi^{J,p}(t_i)\rangle$ is the result from a linear combination of three different possible values of final total angular momentum.

Clearly, it can be seen in equation (17), the three components of $\mu_n (n = -1, 0, 1)$ determine the property of the function $|\varphi_{K,M}^{J',J,p}\rangle$. The components of μ_n can be obtained by projecting the complex conjugate of equations (11) and (12) onto equation (10) namely

$$\mu_n = \boldsymbol{\epsilon}_n^* \cdot \boldsymbol{\mu}. \quad (18)$$

Using the relation in equation (18), now the components μ_n for the parallel transition are given by:

$$\mu_{-1} = \frac{1}{\sqrt{2}}\mu_x, \qquad \mu_0 = \mu_z, \qquad \mu_{+1} = -\frac{1}{\sqrt{2}}\mu_x \quad (19)$$

and for the perpendicular transition are given by:

$$\mu_{-1} = \frac{1}{\sqrt{2}}i\mu_y, \qquad \mu_0 = 0, \qquad \mu_{+1} = \frac{1}{\sqrt{2}}i\mu_y. \quad (20)$$

Employing the relation in equation (19) and the following relation [21,22],

$$\langle j_1,m_1:j_2,-m_2|j_3,-m_3\rangle$$
$$= (-1)^{1+j_1+j_3}\langle j_1,m_1:j_2,m_2|j_3,m_3\rangle, \quad (21)$$

with some manipulations, equation (17) can be reduced to:

$$|\varphi_{K,M}^{J',J,p}(\theta,\omega)\rangle = \frac{1}{4\pi}\sqrt{\frac{2J+1}{(1+\delta_{0,K})}}\frac{1}{\sqrt{2}}|\Theta_{j,K}(\theta)\rangle$$

$$\times \Big\{ -\mu_x\Big[\langle 1,1:J,K|J',1+K\rangle$$

$$\times \Big(D_{1+K,m+M}^{J'}(\omega) + (-1)^{J'+(1+K)+p+1}$$

$$\times D_{-(1+K),m+M}^{J'}(\omega)\Big) + (-1)^{J+J'}$$

$$\times \langle 1,1:J,-K|J',1-K\rangle$$

$$\times \Big(D_{K-1,m+M}^{J'}(\omega) + (-1)^{J'+(K-1)+p+1}$$

$$\times D_{-(K-1),m+M}^{J'}(\omega)\Big)\Big]$$

$$+ \mu_z\langle 1,0:J,K|J',K\rangle\sqrt{2}\Big(D_{K,m+M}^{J'}(\omega)$$

$$+ (-1)^{J'+K+p+1} D_{-K,m+M}^{J'}(\omega)\Big)\Big\}. \quad (22)$$

Making use of the definition in equation (4), separating the $K = 0$ term, equation (22) can be expanded in the following form

$$|\varphi_{K,M}^{J',J,p}(\theta,\omega)\rangle = \sqrt{\frac{2J+1}{2J'+1}}\frac{|\Theta_{j,K}(\theta)\rangle}{\sqrt{2}}(1-\delta_{0,K})$$

$$\times \Big\{ -\mu_x\Big[\langle 1,1:J,K|J',1+K\rangle$$

$$\times \Lambda_{1+K,m+M}^{J',p+1}(\omega) + (-1)^{J+J'}$$

$$\times \langle 1,1:J,-K|J',1-K\rangle$$

$$\times \sqrt{(1+\delta_{0,K-1})}\Lambda_{K-1,m+M}^{J',p+1}(\omega)\Big]$$

$$+ \mu_z\langle 1,0:J,K|J',K\rangle\sqrt{2}\Lambda_{K,m+M}^{J',p+1}(\omega)\Big\}$$

$$+ \sqrt{\frac{2J+1}{2J'+1}}|\Theta_{j,0}(\theta)\rangle\delta_{0,K}$$

$$\times \Big\{ -\mu_x\Big[\langle 1,1:J,0|J',1\rangle \Lambda_{1,m+M}^{J',p+1}(\omega)$$

$$+ (-1)^{J+J'}\langle 1,1:J,0|J',1\rangle \Lambda_{-1,m+M}^{J',p+1}(\omega)\Big]$$

$$+ \mu_z\langle 1,0:J,0|J',0\rangle\sqrt{2}\Lambda_{0,m+M}^{J',p+1}(\omega)\Big\}. \quad (23)$$

Using the fact that $|\Theta_{j,0}(\theta)\rangle = |\Theta_j(\theta)\rangle$, $D_{-1,m+M}^{J'} = -D_{1,m+M}^{J'}$ [21,22] and $(-1)^{J+p} = 1$ when $K = \lambda = 0$,

equation (23) becomes

$$|\varphi_{K,M}^{J',J,p}(\theta,\omega)\rangle = \sqrt{\frac{2J+1}{2J'+1}}\frac{|\Theta_{j,K}(\theta)\rangle}{\sqrt{2}}(1-\delta_{0,K})$$

$$\times \left\{ -\mu_x\Big[\langle 1,1:J,K|J',1+K\rangle \right.$$

$$\times \Lambda_{1+K,m+M}^{J',p+1}(\omega) + (-1)^{J+J'}$$

$$\times \sqrt{(1+\delta_{-1+K})}\,\langle 1,1:J,-K|J',1-K\rangle$$

$$\times \Lambda_{K-1,m+M}^{J',p+1}(\omega)\Big] - \langle 1,0:J,K|J',K\rangle$$

$$\times \mu_z\sqrt{2}\Lambda_{K,m+M}^{J',p+1}(\omega)\Big\}$$

$$+\sqrt{\frac{2J+1}{2J'+1}}|\Theta_j(\theta)\rangle\,\delta_{0,K}$$

$$\times \left\{ -\langle 1,1:J,0|J',1\rangle\,\mu_x\Lambda_{1,m+M}^{J',p+1}(\omega) \right.$$

$$\left. +\langle 1,0:J,0|J',0\rangle\,\mu_z\Lambda_{0,m+M}^{J',p+1}(\omega) \right\}. \tag{24}$$

Using the relation of the Wigner 3-jm symbol

$$\langle j_1,m_1:j_2,m_2|j_3,m_3\rangle = (-1)^{j_1-j_2+m_3}\sqrt{2j_3+1}$$

$$\times \begin{pmatrix} j_1 & j_2 & j_3 \\ m_1 & m_2 & -m_3 \end{pmatrix}, \tag{25}$$

the final form of equation (24) is:

$$|\varphi_{K,M}^{J',J,p}(\theta,\omega)\rangle = \sqrt{2J+1}\frac{|\Theta_{j,K}(\theta)\rangle}{\sqrt{2}}(-1)^{J+K}(1-\delta_{0,K})$$

$$\times \left\{ -\mu_x\left[\begin{pmatrix} 1 & J & J' \\ 1 & K & -1-K \end{pmatrix}\Lambda_{1+K,m+M}^{J',p+1}(\omega) \right.\right.$$

$$+(-1)^{J'+K}\sqrt{(1+\delta_{-1+K})}$$

$$\left.\times \begin{pmatrix} 1 & J & J' \\ 1 & -K & -1+K \end{pmatrix}\Lambda_{K-1,m+M}^{J',p+1}(\omega)\right]$$

$$\left. +\begin{pmatrix} 1 & J & J' \\ 0 & K & -K \end{pmatrix}\mu_z\sqrt{2}\Lambda_{K,m+M}^{J',p+1}(\omega)\right\}$$

$$-(-1)^J\sqrt{2J+1}|\Theta_j(\theta)\rangle\,\delta_{0,K}$$

$$\times \left\{ \begin{pmatrix} 1 & J & J' \\ 1 & 0 & -1 \end{pmatrix}\mu_x\Lambda_{1,m+M}^{J',p+1}(\omega) \right.$$

$$\left. +\begin{pmatrix} 1 & J & J' \\ 0 & 0 & 0 \end{pmatrix}\mu_z\Lambda_{0,m+M}^{J',p+1}(\omega)\right\}. \tag{26}$$
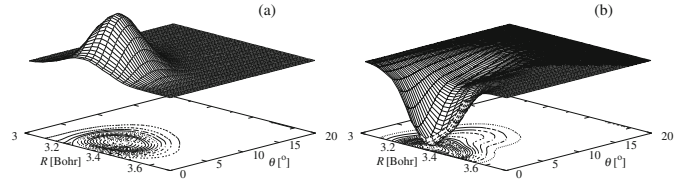
Fig. 6. (a) Real part of $|\varphi_0^{1,0,1}\rangle$, (b) real part of $|\varphi_1^{1,0,1}\rangle$ components of the initial wave packet $|\Phi^{0,1}(t_i)\rangle$, evolving on the $2^1A'$ potential with the N_2O molecule starting from the $(0,0^0,0)$ vibrational state.

Interestingly for the parallel transition, the parity-adapted function in equation (26) has changed to $\Lambda^{J',p+1}$ in the final state from $\Lambda^{J,p}$ in the initial state (4) due to parity conservation of the total wave function where the parity of the nuclear wave function must change upon absorption of a photon. In the current case, the space-fixed z-axis is specified by the direction of ϵ_m for linearly polarized light where m is set to be 0. It can be seen also in equation (26), the initial wave packet $|\Phi^{J,p}(t_i)\rangle$ is constructed from a real function $|\varphi_{K,M}^{J',J,p}\rangle$. Figures 6a and 6b provide examples of the real part of the initial wave packets, associated with two possible values of $K = 0$ and $K = 1$, at a fixed $J' = 1$.

Employing the relations in equations (20) and (21), the function in equation (17) can be written as:

$$|\varphi_{K,M}^{J',J,p}(\theta,\omega)\rangle = \frac{1}{4\pi}\sqrt{\frac{2J+1}{(1+\delta_{0,K})}}|\Theta_{j,K}(\theta)\rangle$$

$$\times \left\{ \frac{i}{\sqrt{2}}\mu_y\left[D_{-1+K,m+M}^{J'}(\omega) \right.\right.$$

$$\times \langle 1,-1:J,K|J',K-1\rangle + (-1)^{J+K+p}$$

$$\times D_{-1-K,m+M}^{J'}(\omega)(-1)^{1+J+J'}$$

$$\left.\times \langle 1,1:J,K|J',1+K\rangle \right]$$

$$+\frac{i}{\sqrt{2}}\mu_y\left[D_{1+K,m+M}^{J'}(\omega) \right.$$

$$\times \langle 1,1:J,K|J',1+K\rangle$$

$$+(-1)^{J+K+p}D_{1-K,m+M}^{J'}(\omega)$$

$$\left.\left.\times \langle 1,1:J,-K|J',1-K\rangle \right]\right\}. \tag{27}$$

Making use of the definition in equation (4), separating the $K = 0$ term, equation (27) can be simplified in

the following form:

$$
\begin{aligned}
|\varphi_{K,M}^{J',J,p}(\theta,\omega)\rangle = {} & \frac{1}{4\pi}\sqrt{\frac{2J+1}{(1+\delta_{0,K})}}\frac{i}{\sqrt{2}}|\Theta_{j,K}(\theta)\rangle \\
& \times \mu_y\Big\{ \langle 1,1:J,K|J',1+K\rangle \\
& \times \Big(D_{1+K,m+M}^{J'}(\omega) + (-1)^{J'+(1+K)+p} \\
& \times D_{-(1+K),m+M}^{J'}(\omega)\Big) + (-1)^{J+J'+1} \\
& \times \langle 1,1:J,-K|J',1-K\rangle \\
& \times \Big(D_{K-1,m+M}^{J'}(\omega) + (-1)^{J'+(K-1)+p} \\
& \times D_{-(K-1),m+M}^{J'}(\omega)\Big)\Big\}.
\end{aligned} \tag{28}
$$

Using the same way of manipulation as in equation (24), equation (28) can be written as:

$$
\begin{aligned}
|\varphi_{K,M}^{J',J,p}(\theta,\omega)\rangle = {} & \sqrt{\frac{2J+1}{2J'+1}}\frac{i\,|\Theta_{j,K}(\theta)\rangle}{\sqrt{2}}\mu_y\,(1-\delta_{0,K}) \\
& \times \Big\{ \langle 1,1:J,K|J',1+K\rangle \Lambda_{1+K,m+M}^{J',p}(\omega) \\
& + \sqrt{(1+\delta_{0,-1+K})}\,(-1)^{J+J'+1} \\
& \times \langle 1,1:J,-K|J',1-K\rangle \Lambda_{K-1,m+M}^{J',p}(\omega)\Big\} \\
& + i\sqrt{\frac{2J+1}{2J'+1}}|\Theta_j(\theta)\rangle\,\mu_y\delta_{0,K} \\
& \times \langle 1,1:J,0|J',-1\rangle \Lambda_{1,m+M}^{J',p}(\omega).
\end{aligned} \tag{29}
$$

Using the relation of (25), equation (29) becomes

$$
\begin{aligned}
|\varphi_{K,M}^{J',J,p}(\theta,\omega)\rangle = {} & \sqrt{2J+1}\frac{i\,|\Theta_{j,K}(\theta)\rangle}{\sqrt{2}} \\
& \times \mu_y(-1)^{J+K}\,(1-\delta_{0,K}) \\
& \times \Big\{ \begin{pmatrix} 1 & J & J' \\ 1 & K & -1-K \end{pmatrix} \Lambda_{1+K,m+M}^{J',p}(\omega) \\
& - \sqrt{(1+\delta_{0,-1+K})}\,(-1)^{J'+K} \\
& \times \begin{pmatrix} 1 & J & J' \\ 1 & -K & -1+K \end{pmatrix} \Lambda_{K-1,m+M}^{J',p}(\omega)\Big\} \\
& + i\sqrt{2J+1}|\Theta_j(\theta)\rangle\,\mu_y\delta_{0,K}(-1)^{J} \\
& \times \begin{pmatrix} 1 & J & J' \\ 1 & 0 & 1 \end{pmatrix} \Lambda_{1,m+M}^{J',p}(\omega).
\end{aligned} \tag{30}
$$

By comparing functions in equation (26), conversely, the parity-adapted function for the perpendicular transition in
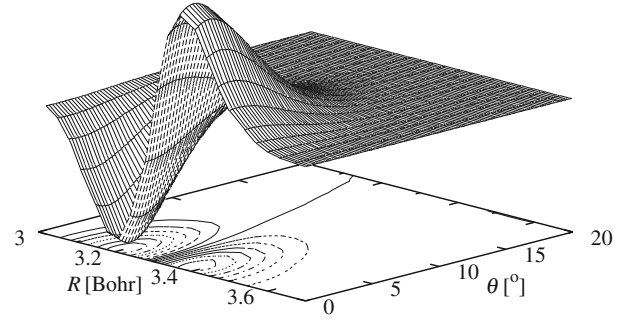
Fig. 7. Imaginary part of the $|\varphi_1^{1,0,2}\rangle$ component of the initial wave packet $|\Phi^{0,2}(t_i)\rangle$, evolving on the $1^1A''$ potential with the N_2O molecule starting from the $(0,0^0,0)$ vibrational state.

equation (30) remains unchanged to $\Lambda^{J',p}$ in the final state from $\Lambda^{J,p}$ in the initial state (4) due to parity conservation of the total wave function. For determination of the space-fixed z-axis, a similar set up of $m = 0$ was used. Contrary to the parallel transition, the initial wave packet for the perpendicular transition is constructed from an imaginary function $|\varphi_{K,M}^{J',J,p}\rangle$. Figure 7 provides an example of the imaginary part of the initial wave packet, associated with $K = 1$ and $J' = 1$.

For the initial vibrational state with odd bending quantum number, only $J = 1$ was considered because $J = 0$ is forbidden by symmetry. Nevertheless, for even bending quantum number, only $J = 0$ was considered.

2.3 Wave packet at t > 0

By solving the time-dependent Schrödinger equation, the wave packet at time $t > 0$ is obtained as:

$$
|\Phi^{J,p}(t)\rangle = \exp\left(\frac{i\hat{H}t}{\hbar}\right)|\Phi^{J,p}(t_i)\rangle \tag{31}
$$

where $\hat{H}$ is the full upper surface Hamiltonian given by equation (5). In order to propagate the wave packet $\Phi^{J,p}$ in time, we employed a propagator based on the complex Chebyshev polynomial series.

Since the Chebyshev polynomial is bounded in the interval $(-1,1)$, the Hamiltonian has to be renormalized in such a way that

$$
\hat{H}_{\mathrm{norm}} = \frac{2}{\Delta E}\left\{ \hat{H} - \hat{I}\left(\frac{\Delta E}{2} + V_{\min}\right)\right\} \tag{32}
$$

where $\Delta E = E_{\max} - E_{\min}$. As proposed by Tal-Ezer and Kosloff [28], the propagator is given by:

$$
\begin{aligned}
\exp\left(\frac{-i\hat{H}t}{\hbar}\right) = {} & \exp\left\{\frac{-i}{\hbar}\left(\frac{\Delta E}{2} + V_{\min}\right)t\right\} \\
& \times \sum_{n=0}^{N}(2-\delta_{n,0})J_n\left(\frac{\Delta E t}{2\hbar}\right) \\
& \times C_n(-i\hat{H}_{\mathrm{norm}})
\end{aligned} \tag{33}
$$
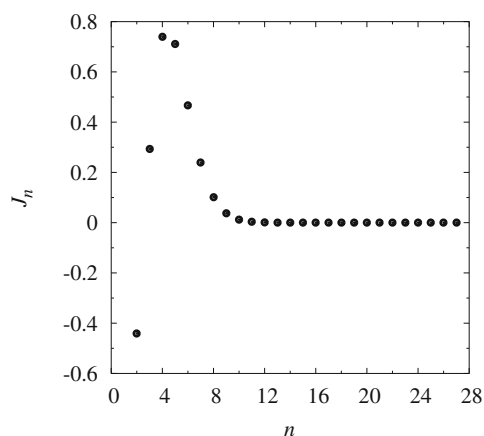
Fig. 8. Convergence of Bessel function (J_n) with respect to the number of terms (n) used in Chebyshev expansion.

where J_n are the Bessel functions of the first kind of order n and C_n are complex Chebyshev polynomials satisfying the recurrence relation [29]

$$A_{n+1} = -2i\hat{H}_{\mathrm{norm}}A_n + \Gamma_{n-1} \text{ for } n = 1, 2, \ldots, N-1 \quad (34)$$

with Γ is related to the initial wave packet by

$$A_n = C_n(-i\hat{H}_{\mathrm{norm}})\,|\Phi^{J,p}(R, r, \theta, \omega, t_i)\rangle. \quad (35)$$

The Bessel function $J_n(\Delta E t/2\hbar)$ falls off to zero exponentially as n becomes greater than $\Delta E t/2\hbar$. This happens rapidly for larger $\Delta E t/2\hbar$ and one needs to include only a few extra terms above $n = \Delta E t/2\hbar$ for convergence. The number of terms n used in the Chebyshev expansion was 27. Figure 8 shows the Bessel function is satisfactorily converged to zero for a n value of 27. The wave packet was propagated using the Chebychev propagator, on an equally spaced grid that ranges from 1 to 14 Bohr with a step size of 0.03385 Bohr. For a molecule with initial $J = 1$, calculation with specific total angular momentum J', and parity was performed separately because different values of J' and parity do not couple during propagation of the wave packet. In contrast, the helicity quantum number K is not conserved and different values of K are coupled during propagation via equation (16).

The propagated wave packet $\Phi^{J,p}(t)$ contains non-zero values in both of the real and imaginary parts which is due to the complex argument in the time propagator in equation (33). Figure 9 displays the contribution of different wave packet components corresponding to different values of K at time 10 a.u. propagated on the $2^1A'$ surface. Apparently, the magnitude of both of the real and imaginary parts of the wave packets are located at the same phase. On the contrary, Figure 10 depicts the magnitude of both of the real and imaginary parts as being located at different phases when the wave packet evolves on the $1^1A''$ surface.
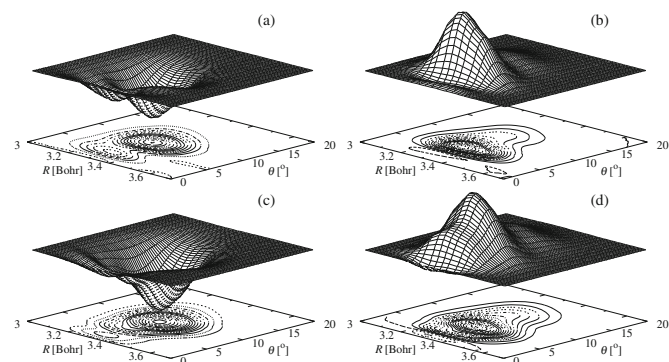
Fig. 9. (a) Real part of $\varphi_0^{1,0,1}$, (b) real part of $\varphi_1^{1,0,1}$, (c) imaginary part of $\varphi_0^{1,0,1}$, (d) imaginary part of $\varphi_1^{1,0,1}$ components of the wave packet $\Phi^{0,1}$ ($t = 10$), evolving on the $2^1A'$ potential with the N_2O molecule starting from the $(0,0^0,0)$ vibrational state.
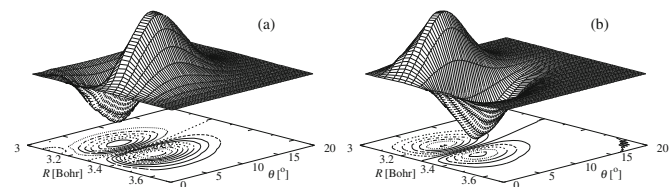
Fig. 10. (a) Real part of $\varphi_1^{1,0,2}$, (b) real part of $\varphi_1^{1,0,2}$ components of the wave packet $\Phi^{0,2}$ ($t = 10$), evolving on the $1^1A''$ potential with the N_2O molecule starting from the $(0,0^0,0)$ vibrational state.

3 Results and discussion

Using the computed potential energy and transition dipole moments surfaces, the total photoabsorption cross sections as a function of incident wavelength were calculated for transitions from the X^1A' ground electronic state to the two lowest $2^1A'$ and $1^1A''$ excited electronic states. The energy dependence of the total cross section is related to the Fourier transform of the autocorrelation function as given by equation (1). Figure 11 depicts two examples of the autocorrelation function as a function of time, obtained by computing the overlap of the evolving wave packet $\Phi^{J,p}(t)$ with $\Phi^{J,p}(t_i)$. We found that the cross section is very sensitive to the shape and the magnitude of the transition dipole moment in the Franck-Condon region.

Figures 12 and 13 illustrate the contribution of all different possible values of the final total angular momentum to the total absorption cross section for the $X^1A' \rightarrow 2^1A'$ and $X^1A' \rightarrow 1^1A''$ transitions when the molecule starts from $J = 1$. The total cross sections displayed for $J = 1$ are obtained by summing over all allowed values of the final state of total angular momentum. Apparently, for the $X^1A' \rightarrow 2^1A'$ parallel transition, the intensity of the total cross section gradually increases with increasing J'. While for the $X^1A' \rightarrow 1^1A''$ perpendicular transition, the two values of J', 1 and 2, more or less contribute equally to the total absorption cross section.

The photoabsorption of N_2O from the ground state X^1A' to the second lowest excited state $2^1A'$ is a direct process and therefore the fragments immediately start to
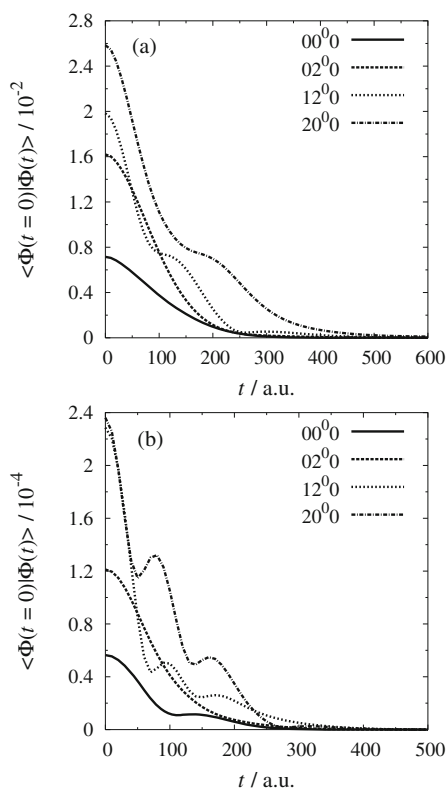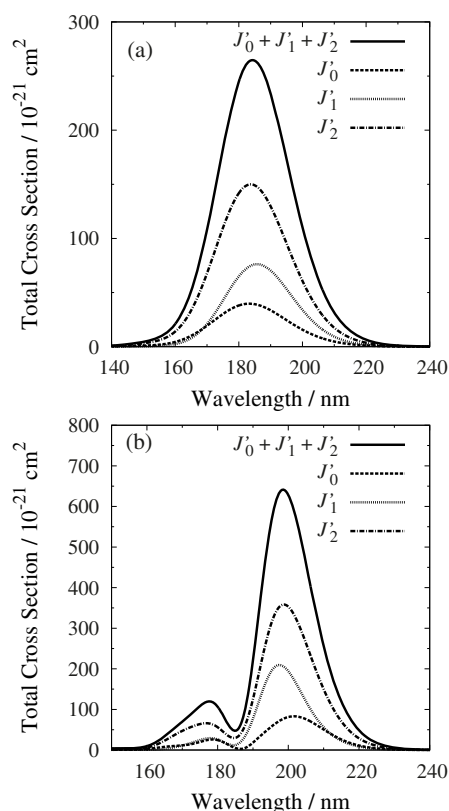
Fig. 11. Autocorrelation functions for the two lowest transitions: (a) $X^1A' \rightarrow 2^1A'$; (b) $X^1A' \rightarrow 1^1A''$. The N_2O molecule is initially in its $(0,0^0,0)$, $(0,2^0,0)$, $(1,2^0,0)$ and $(2,0^0,0)$ vibrational states with total angular momentum $J = 0$, even parity $(p = 2)$.

Fig. 12. Contribution of different final total angular momentum ($J'_0 = 0$, $J'_1 = 1$ and $J'_2 = 2$) to the total absorption cross section ($J'_0 + J'_1 + J'_2$) for the $X^1A' \rightarrow 2^1A'$ transition with the N_2O molecule starting from different initial vibrational states: (a) $(0,1^1,0)$; (b) $(1,1^1,0)$. The initial total angular momentum is $J = 1$, odd parity $(p = 1)$.

separate once N_2O is created in the excited electronic state. After about 600 a.u. the process is essentially completed (see Fig. 11a). The wave packet follows mainly the path of steepest descent from the Franck-Condon region out into the N_2-O exit channel. Total absorption cross sections resulting from different initial vibrational and rotational states are plotted in Figure 14. The absorption line shapes can be seen to be basically structureless. The most attractive feature of the time-dependent wave packet is that a single propagation of the wave packet, i.e. one single solution of the time-dependent Schrödinger equation automatically yields the total absorption cross section over a large range of energy.

Absorption from initial levels of the pure bending vibration $(0,0^0,0)$, $(0,1^1,0)$, $(0,2^0,0)$ and $(0,3^1,0)$ result in single-peaked cross sections. These cross sections are depicted in Figure 14a. Figure 11a depicts the corresponding autocorrelation functions for some of the initial bending states. Since the dissociation is direct, the autocorrelation function decays monotonically to zero without showing any recurrence at larger times. The dissociation is rather slow because the potential slope out to bending coordinates is flat between $\theta = 0°$ and $\theta = 5°$. Moreover, the fairly light O atom is ejected like a discuss due to the torque generated by the anisotropy of the $2^1A'$ potential energy surface for N_2-O bending angles greater than

5°, leaving the N_2 fragments spinning very fast about its center-of-mass and most of the available energy goes into rotation rather than translation. The absorption cross section will thus simply be a slightly broad featureless curve centered on the mean energy with a width ($\Delta E = \hbar/\Delta t$) that reflects the time taken for the wave packet to leave the Franck-Condon region.

Absorption cross sections arising from different initial pure N-O stretching modes $(1,0^0,0)$ and $(2,0^0,0)$ result in different numbers of nodal structures. Both cross sections are shown in Figure 14b. The structures are in a very qualitative view, a reflection of the nodal pattern of the bound vibrational wave function. For instance, the wave function of the $(2,0^0,0)$ state has two nodes along the propagation route which clearly show up in the cross section as well. The corresponding structures as shown in the autocorrelation function (see Fig. 11b) are due to the nodal structure of the initial wave function rather than a recurrence of the evolving wave packet. When $\Phi(t)$ starts to evolve in time and space the overlap with $\Phi(t_i)$ becomes slightly modulated. Nonetheless, this picture becomes certainly more complicated as the degree of vibrational excitation increases.

The autocorrelation function from a bending excitation does not exhibit any structure originating from
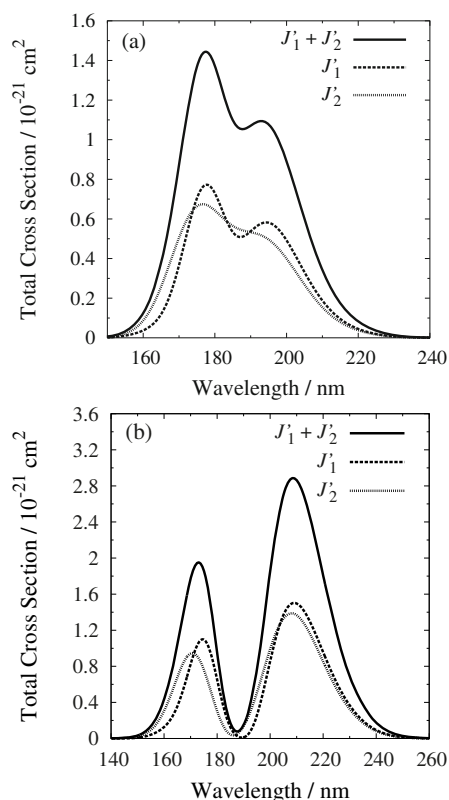
Fig. 13. Contribution of different final total angular momentum ($J'_1 = 1$ and $J'_2 = 2$) to the total absorption cross section ($J'_1 + J'_2$) for the $X^1A' \rightarrow 1^1A''$ transition with the N_2O molecule starting from different initial vibrational states: (a) $(0,1^1,0)$; (b) $(1,1^1,0)$. The initial total angular momentum $J = 1$, odd parity ($p = 1$).

the nodal structure of the bound state wavefunction. It was found that only the nodes along the N_2-O stretching coordinate, do not cause structures in the cross section. Nodes along the N_2-O bending coordinate, on the other hand, lead to reflection structures. The cross sections in Figure 14c, $(1,1^1,0)$ and $(1,2^0,0)$, support this interpretation namely the bending state quantum number increases from one to two, but the number of nodes in the cross section remains unchanged. In other word, the structure in Figure 14c solely depends on the stretching mode wave function, on the other hand, the bending mode greatly influences the intensity of the cross section.

Generally, the effect of pure bending excitation substantially increases the intensity of the cross section. The effect is similar for the transition from pure stretching and coupled bending-stretching states. Nevertheless, there is an exception for the case of two quanta of bending vibration $(0,2^0,0)$ in which the resultant cross section is lower than that of the one quantum of bending vibration $(0,1^1,0)$. In this regard, our result differs to that reported by Schinke in Figure 12 from reference [30]. He shows that the intensity of the $(0,2^0,0)$ cross section is far higher than for $(0,1^1,0)$. We believe that our result is more accurate, supported by a similar pattern in Figure 14c in which the $(1,2^0,0)$ cross section is lower than that of the $(1,1^1,0)$ cross
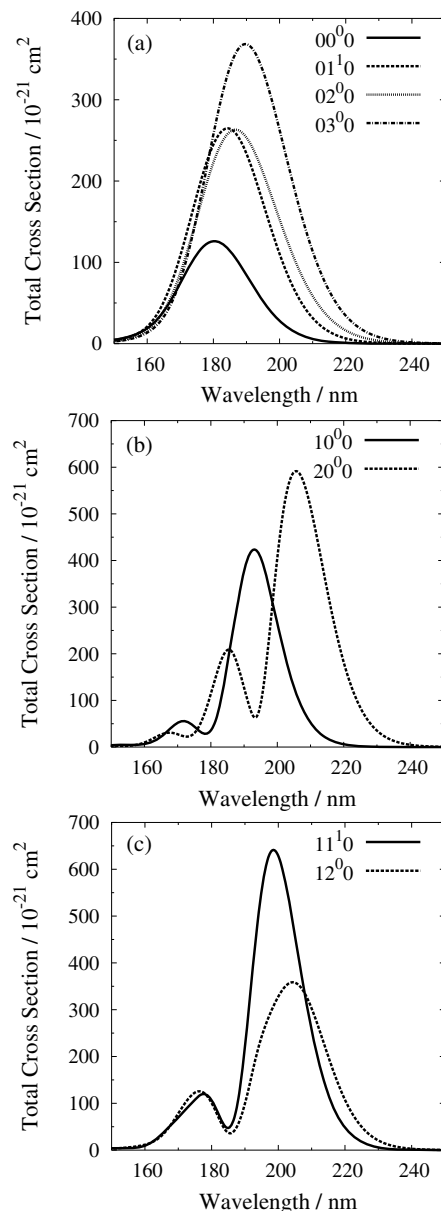
Fig. 14. Total absorption cross section for the $X^1A' \rightarrow 2^1A'$ transition with the N_2O molecule starting from different initial vibrational states: (a) ground state $(0,0^0,0)$ and excited states of pure bending modes $(0,1^1,0)$, $(0,2^0,0)$ and $(0,3^1,0)$; (b) excited states of pure stretching modes $(1,0^0,0)$ and $(2,0^0,0)$; (c) excited states of coupled bending-stretching modes $(1,1^1,0)$ and $(1,2^0,0)$.

section. In order to understand the general shape and the intensity of the cross section, it is mandatory also to take into account the coordinate dependence of the transition dipole function. Since the transition dipole rises toward larger bond angle, the cross section generally increases and becomes wider. Not surprisingly, due to the complexity of the function particularly in the Franck-Condon region, the excitation strength from the $(0,2^0,0)$ state is slightly weaker than the $(0,1^1,0)$ state.
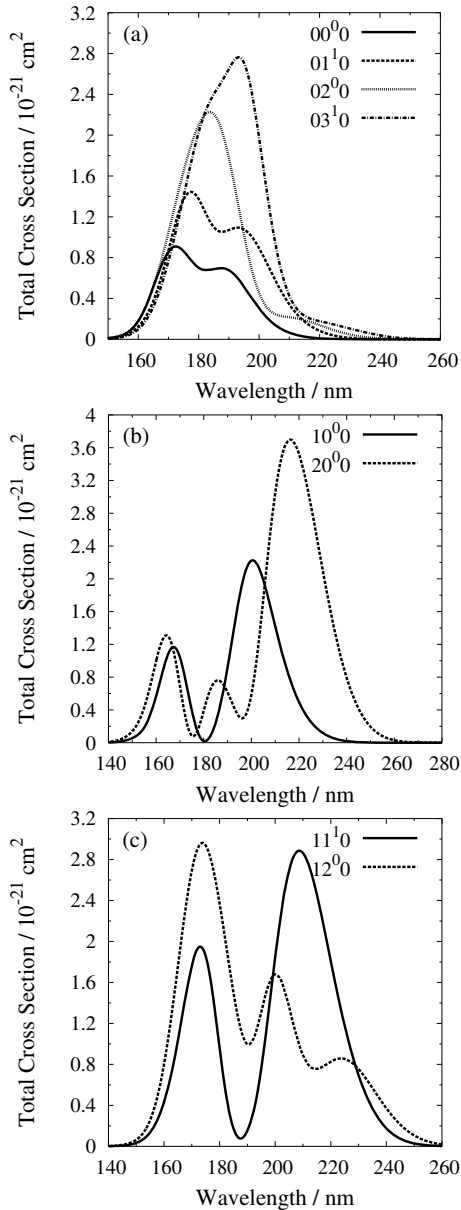
Fig. 15. Total absorption cross section for the $X^1A' \rightarrow 1^1A''$ transition with the N_2O molecules starting from different initial vibrational states: (a) ground state $(0,0^0,0)$ and excited states of pure bending modes $(0,1^1,0)$, $(0,2^0,0)$ and $(0,3^1,0)$; (b) excited states of pure stretching modes $(1,0^0,0)$ and $(2,0^0,0)$; (c) excited states of coupled bending-stretching modes $(1,1^1,0)$ and $(1,2^0,0)$.

Figure 15 depicts the total absorption cross section for the transition to the $1^1A''$ state from different initial rotational-vibrational ground states. Generally, they are more structured than the $2^1A'$ cross section. Basically, the same trends can be seen as observed for the case of $2^1A'$ with only one notable exception. A couple of similarities are not surprising due to the resemblance of the topography between the two surfaces. Absorption to the $1^1A''$ state from the two lowest bending vibrational states $(0,0^0,0)$ and $(0,1^1,0)$ results in a two-peaked cross section.

This double hump structure has nothing to do with the reflection of the bending wave function in the ground state, as previously discussed for the reflection of the stretching mode wave function. It is a consequence of the node in the transition dipole moment function near equilibrium collinear geometry $\theta = 1°$ and $R = 3.35$ Bohr, displayed in Figure 4. The node coincides with the node of the initial wave packet as can be seen in Figure 7. The double hump structure, nevertheless, is damped with increasing bending quantum number, since the breadth of the bending wave function becomes larger and the initial wave packet samples more and more the strongly anisotropic portion of the potential energy surface.

The manner in which only one component μ_x of the $2^1A'$ transition dipole moments (i.e. μ_x and μ_z) cross zero has produced a quite smooth change in the magnitude of the transition dipole moment. It can be said that a node of the initial wave packet on the $2^1A'$ potential energy surface is washed out along the N-O coordinate simply because the effect of the zero transition dipole of one component μ_x is cancelled by the non-zero one of the other component μ_z. Mathematically, the exact relation between the two components μ_x and μ_z is derived through equation (26), but a simple qualitative picture is difficult to extract.

For comparison with experimental spectra, the total absorption cross section of each transition to two lowest absorption bands has been computed from contributions of initial states $(0,0^0,0)$, $(0,1^1,0)$, $(0,2^0,0)$, $(1,0^0,0)$, $(0,3^1,0)$ and $(1,1^1,0)$ at a room temperature of 297 K. A Boltzmann average of cross sections over initial vibrational states is given by:

$$
\sigma_{2^1A'/1^1A''}(T) = \left(\sigma_{000} + 2\sigma_{010}e^{\Gamma_{010}} + 3\sigma_{020}e^{\Gamma_{020}} \right.
$$
$$
+ \sigma_{100}e^{\Gamma_{100}} + 4\sigma_{030}e^{\Gamma_{030}} + \sigma_{110}e^{\Gamma_{110}} \left. \right) /
$$
$$
\left(1 + 2e^{\Gamma_{010}} + 3e^{\Gamma_{020}} + e^{\Gamma_{100}} \right.
$$
$$
\left. + 4e^{\Gamma_{030}} + e^{\Gamma_{110}} \right), \tag{36}
$$

where

$$
\Gamma_{ijk} = \frac{-\epsilon_{ijk}}{kT}, \tag{37}
$$

k is the Boltzmann constant, T is the temperature in Kelvin, ϵ $(\equiv \Delta E_i)$ is vibrational energy of the ground state (refer to Tab. 1) and the coefficients 1, 2, 3 and 4 are used to account for the degeneracy of the states $(0,0^0,0)$, $(0,1^1,0)$, $(0,2^0,0)$ and $(0,3^1,0)$. Finally, the total absorption cross section is constructed from the sum over the Boltzmann averaged absorption line shapes of the two lowest excited states $2^1A'$ and $1^1A''$:

$$
\sigma_{total}(T) = \sigma_{2^1A'}(T) + \sigma_{1^1A''}(T). \tag{38}
$$

At 297 K, we found that almost 100% of the population of N_2O is in the ground state $(0,0^0,0)$ and one quantum of bending vibration $(0,1^1,0)$. Moreover, there is a substantial contribution due to hot-band excitation from the $(0,1^1,0)$ vibrationally excited state, which is in accordance with previous experimental measurements of the temperature-dependent absorption spectrum by
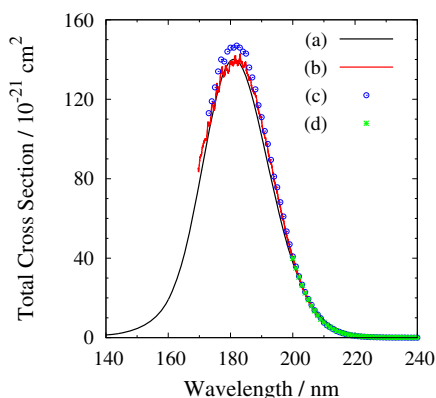
Fig. 16. Comparison between the calculated total absorption cross section and the experimental spectrum of the N_2O molecule. (a) Calculated cross section; (b) measured by Yoshino et al. (297 K) [32]; (c) measured by Selwyn and Johnston (298 K) [33,35]; (d) measured by Merienne et al. (296 K) [34]. The theoretical cross section is calculated from the contribution of the two lowest excited states, $2^1A'$ and $1^1A''$. Each total absorption cross section of the excited states is obtained by Boltzmann averaging at 297 K of six total cross sections with the N_2O molecule initially in its $(0,0^0,0)$, $(0,1^1,0)$, $(0,2^0,0)$, $(1,0^0,0)$, $(0,3^1,0)$ and $(1,1^1,0)$ vibrational states.
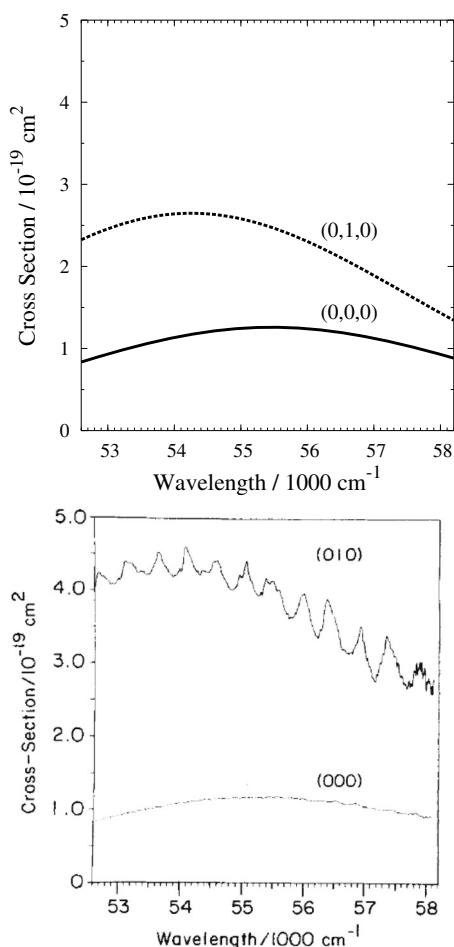
Selwyn and Johnston [31]. The total absorption cross section σ_{total} from the contribution of two excited states is plotted in Figure 16, along with the experimentally measured high resolution ultraviolet absorption spectrum obtained by Yoshino et al. [32] from photolysis of N_2O in the wavelength region 170–220 nm at a temperature of 297 K. In general, the calculated absorption cross section is in excellent quantitative agreement with the experimental spectrum in respect of, both the absolute value of the cross section and the position of the maximum absorption peak, and of the overall shape of the cross section. The absolute value of the spectrum measured by Yoshino et al. has been confirmed by three independent experimental results [33–35], and, hence, the value should be correct for comparison purposes. The diffuse structures are absent in the cross section which was attributed by Schinke [30] to N-N streching vibration. By considering the N-N dimension, the structures were seen in their three-dimensional calculation. However, their cross section has been multiplied by 1.37 to shift the cross section upward by 0.05×10^{-19} cm^2 in order to reproduce the same intensity as found in the experimental spectrum. Meanwhile, the three-dimensional calculation by Nanbu and Johnson [36] yielded a rather narrow cross section in logarithmic scale near the absorption peak. Simplification in their calculation by taking the final angular momentum to be zero only is not enough to reproduce the experimental cross section. Now it is clear from these two pieces of evidence that the full-dimensional dynamics approach is not sufficient to produce accurate values of the cross section without having considered all aspects of angular momemtum coupling. Surprisingly, our current reduced dimensionality model with proper treatment of angular momentum coupling has produced better results when

compared to them and to our previous two dimensional result [37]. Nevertheless, it cannot be denied that the three-dimensional model has produced vibrationally diffuse structures around the absorption peak very well due to the N-N vibrational effects.

The likelihood of hot-band excitation being involved in the photoabsorption of N_2O is indicated by a number of experimental measurements. The increase in the total cross section for absorption from the initial vibrational state $(0,1^1,0)$ and its shift to longer wavelengths relative to the $(0,0^0,0)$ cross section quantitatively agrees well with the experimental results of the temperature-dependent absorption spectrum reported by Selwyn and Johnston [31]. They measured the absorption spectrum at 151 K peaking at $55\,000$ cm^{-1} (181.8 nm) with a maximum value of approximately 110×10^{-21} cm^2 and, they attributed this spectrum as providing a good approximation for excitation from the pure $(0,0^0,0)$ state. Current work supports their approximation very well, as depicted in Figure 17 of the $(0,0^0,0)$ cross section. For the sake of comparison, Figure 17 also displays the deconvoluted experimental spectrum adopted from the paper by Selwyn and Johnston [31]. By deconvoluting spectra at five difference temperatures and using an appropriate weighting factor (see Ref. [31] for details), the resultant spectrum displays a peak at $54\,400$ cm^{-1} (183.8 nm) with a maximum value of approximately 425×10^{-21} cm^2 which represents a spectrum from the hot-band excitation of the pure $(0,1^1,0)$ state. Noted that the structures appear in the (0 1 0) spectrum was not found in the calculation due to the reduced dimensionality applied by keeping N-N fixed at its equilibrium geometry. This has been discussed in the earlier paragraph in which the structures are related to the N-N vibrational motion during dissociation. Our ratio $\sigma_{(0,0^0,0)}/\sigma_{(0,1^1,0)}$ of the position of the maximum peak is in excellent agreement with that measured by Selwyn and Johnston. However, our ratio $\sigma_{(0,0^0,0)}/\sigma_{(0,1^1,0)}$ of the absolute values of the maximum peak is underestimated by a factor of 0.45 due to the discrepancy in the $(0,1^1,0)$ cross section.

4 Conclusion

Present work shows that through a correct ab initio representation of the dynamics of photoabsorption processes, it is possible to obtain essentially quantitative agreement between theoretical results and the experimental observation. A detailed discussion of the angular momentum theory required for two kinds of photoabsorption processes has been presented, emphasizing: (a) the correct combination of initial and final parities and total angular momenta; (b) the relative contributions of each of the helicity quantum numbers which are coupled to each other during wave packet propagation. Selecting a single initial rotational and vibrational state from various modes allows us to characterize the controlling role of the potential energy and transition dipole moment surfaces on the dynamics of the model system $N_2O + h\nu \rightarrow N_2 + O$. Our calculations revealed that a large contribution of the transition

Fig. 17. Comparison between the calculated total absorption cross section (upper panel) and the experimental spectrum (lower panel) of the N_2O molecule measured by Selwyn and Johnston [31]. Each of the theoretical cross sections (upper panel) of the N_2O molecule starting from the initial $(0,0^0,0)$ and $(0,1^1,0)$ vibrational states are calculated from the contribution of two lowest excited states, $2^1A'$ and $1^1A''$.

dipole lies on the molecular plane parallel to the direction of the N-O bond in accord with a large positive anisotropy parameter (β) observed for nearly all of the N_2 levels experimentally [10–18]. In general, the resulting total cross section reported here is in excellent agreement with the experimental observation and thus provides a quantitative test of the method.

References

1. E.J. Heller, J. Chem. Phys. **68**, 2066 (1978)
2. R. Kosloff, J. Phys. Chem. **92**, 2087 (1988)
3. Z. Bacic, J.C. Light, Ann. Rev. Phys. Chem. **40**, 469 (1989)
4. C. Light, I.P. Hamilton, V.J. Lill, J. Chem. Phys. **82**, 1400 (1985)
5. D. Neuhauser, M. Baer, R.S. Judson, D.J. Kouri, J. Chem. Phys. **93**, 312 (1990)
6. R.S. Judson, D.J. Kouri, D. Neuhauser, M. Baer, Phys. Rev. A **42**, 351 (1990)
7. D.H. Zhang, J.Z.H. Zhang, J. Chem. Phys. **101**, 1146 (1994)
8. R.C. Mowrey, D.J. Kouri, J. Chem. Phys. **84**, 6466 (1986)
9. M.N. Daud, G.G. Balint-Kurti, Chin. Phys. Lett. **26**, 073302 (2009)
10. T.F. Hanisco, A.C. Kummel, J. Phys. Chem. **97**, 7242 (1993)
11. D.W. Neyer, A.J.R. Heck, D.W. Chandler, J. Chem. Phys. **110**, 3411 (1999)
12. D.W. Neyer, A.J.R. Heck, D.W. Chandler, J.M. Teule, M.H.M. Janssen, J. Phys. Chem. A **103**, 10388 (1999)
13. T. Suzuki, H. Katayanagi, K. Mo Y. Tonokura, Chem. Phys. Lett. **256**, 90 (1996)
14. P. Felder, B.M. Haas, J.R. Huber, Chem. Phys. Lett. **186**, 177 (1991)
15. N. Shafer, K. Tonokura, Y. Matsumi, S. Tasaki, J. Chem. Phys. **95**, 6218 (1991)
16. L.L. Springsteen, S. Satyapal, Y. Matsumi, L.M. Dobeck, J. Phys. Chem. **97**, 7239 (1993)
17. J.M. Teule, G.C. Groenenboom, D.W. Neyer, D.W. Chandler, M.H.M. Janssen, Chem. Phys. Lett. **320**, 177 (2000)
18. M. Ahmed, E.R. Wouters, D.S. Peterka, O.S. Vasyutinskii, Faraday Disc. **113**, 425 (1999)
19. T.H. Dunning Jr., J. Chem. Phys. **90**, 1007 (1989)
20. R.D. Amos, A. Bernhardsson, A. Berning, P. Celani, D.L. Cooper, M.J.O. Deegan, A.J. Dobbyn, F. Eckert, C. Hampel, G. Hetzer, P.J. Knowles, T. Korona, R. Lindh, A.W. Lloyd, S.J. McNicholas, F.R. Manby, W. Meyer, M.E. Mura, A. Nicklass, P. Palmieri, R. Pitzer, G. Rauhut, M. Schütz, U. Schumann, H. Stoll, A.J. Stone, R. Tarroni, T. Thorsteinsson, H.-J. Werner, MOLPRO, a package of ab initio programs designed by H.-J. Werner and P.J. Knowles version 2002.1
21. D.A. Varshalovich, A.N. Moskalev, V.K. Khersonskii, *Quantum Theory of Angular Momentum* (World Scientific, Singapore, 1998)
22. R.N. Zare, *Angular Momentum – Understanding Spatial Aspects in Chemistry and Physics* (John Wiley and Sons, New York, 1998)
23. J. Tennyson, B.T. Sutcliffe, J. Chem. Phys. **77**, 4061 (1982)
24. C. Leforestier, J. Chem. Phys. **94**, 6388 (1991)
25. A. Campargue, D. Permogorov, M. Bach, M. Temsamani, J.V. Auwera, M. Fujii, J. Chem. Phys. **103**, 5931 (1995)
26. A. Campargue, Chem. Phys. Lett. **259**, 563 (1996)
27. R.A. Toth, Appl. Opt. **30**, 5289 (1991)
28. H. Tal-Ezer, R. Kosloff, J. Chem. Phys. **81**, 3967 (1984)
29. M. Abramowitz, I.A. Stegun, *Handbook of Mathematical Functions with Formulas, Graphs, and Mathematical Tables* (U.S. Department of Commerce, 1972)
30. R. Schinke, J. Chem. Phys. **134**, 064313 (2011)

31. G.S. Selwyn, H.S. Johnston, J. Chem. Phys. **74**, 3791 (1981)
32. K. Yoshino, D.E. Freeman, W.H. Parkinson, Planet. Space Sci. **32**, 1219 (1984). Spectral data can be downloaded from Harvard-Smithsonian Center for Astrophysics Molecular Data base, http://www.cfa.harvard.edu/amp/ampdata/n2opub84/n2o.html
33. G. Selwyn, J. Podolske, H.S. Johnston, Geophys. Res. Lett. **4**, 427 (1977)
34. M.F. Mérienne, B. Coquart, A. Jenouvrier, Planet. Space Sci. **38**, 617 (1990)
35. W.B. De More, S.P. Sander, C.J. Howard, A.R. Ravishankara, D.M. Golden, C.E. Kolb, R.F. Hampson, M.J. Kurylo, M.J. Molina, *Chemical Kinetics and Photochemical Data for Use in Stratospheric Modeling* (Jet Propulsion Laboratory, California Institute of Technology, Pasadena, 1997)
36. S. Nanbu, M.S. Johnson, J. Phys. Chem. A **108**, 8905 (2004)
37. M.N. Daud, G.G. Balint-Kurti, A. Brown, J. Chem. Phys. **122**, 054305 (2005)